

Structure and evolution of ultra-massive white dwarfs in general relativity[★]

Leandro G. Althaus^{1,2}, María E. Camisassa³, Santiago Torres^{4,5}, Tiara Battich⁶, Alejandro H. Córscico^{1,2}, Alberto Rebassa-Mansergas^{4,5}, and Roberto Raddi^{4,5}

- ¹ Grupo de Evolución Estelar y Pulsaciones, Facultad de Ciencias Astronómicas y Geofísicas, Universidad Nacional de La Plata, Paseo del Bosque s/n, 1900 La Plata, Argentina
e-mail: althaus@fcaglp.unlp.edu.ar
- ² IALP-CCT – CONICET, Facultad de Ciencias Astronómicas y Geofísicas, Paseo del Bosque S/N, B1900FWA La Plata, Argentina
- ³ Applied Mathematics Department, University of Colorado, Boulder, CO 80309-0526, USA
- ⁴ Departament de Física, Universitat Politècnica de Catalunya, c/Esteve Terrades 5, 08860 Castelldefels, Spain
- ⁵ Institute for Space Studies of Catalonia, c/Gran Capita 2–4, Edif. Nexus 104, 08034 Barcelona, Spain
- ⁶ Max-Planck-Institut für Astrophysik, Karl-Schwarzschild-Str. 1, 85748 Garching, Germany

Received 26 July 2022 / Accepted 24 August 2022

ABSTRACT

Context. Ultra-massive white dwarfs ($M_{\star} \gtrsim 1.05 M_{\odot}$) are of utmost importance in view of the role they play in type Ia supernovae explosions, merger events, the existence of high-magnetic-field white dwarfs, and the physical processes in the super asymptotic giant branch phase.

Aims. We aim to present the first set of constant rest-mass ultra-massive oxygen-neon white dwarf cooling tracks with masses of $M_{\star} > 1.29 M_{\odot}$ which fully take into account the effects of general relativity on their structural and evolutionary properties.

Methods. We computed the full evolution sequences of 1.29, 1.31, 1.33, 1.35, and 1.369 M_{\odot} white dwarfs with the La Plata stellar evolution code, LPCODE. For this work, the standard equations of stellar structure and evolution have been modified to include the effects of general relativity. Specifically, the fully general relativistic partial differential equations governing the evolution of a spherically symmetric star are solved in a way so that they resemble the standard Newtonian equations of stellar structure. For comparison purposes, the same sequences have been computed for the Newtonian case.

Results. According to our calculations, the evolutionary properties of the most massive white dwarfs are strongly modified by general relativity effects. In particular, the resulting stellar radius is markedly smaller in the general relativistic case, being up to 25% smaller than predicted by the Newtonian treatment for the more massive ones. We find that oxygen-neon white dwarfs more massive than 1.369 M_{\odot} become gravitationally unstable with respect to general relativity effects. When core chemical distribution due to phase separation on crystallization is considered, such instability occurs at somewhat lower stellar masses, $\gtrsim 1.36 M_{\odot}$. In addition, cooling times for the most massive white dwarf sequences are about a factor of two smaller than in the Newtonian case at advanced stages of evolution. Finally, a sample of white dwarfs have been identified as ideal candidates to test these general relativistic effects.

Conclusions. We conclude that the general relativity effects should be taken into account for an accurate assessment of the structural and evolutionary properties of the most massive white dwarfs. These new ultra-massive white dwarf models constitute a considerable improvement over those computed in the framework of the standard Newtonian theory of stellar interiors.

Key words. stars: evolution – stars: interiors – white dwarfs

1. Introduction

White dwarf stars are the most common end point of stellar evolution. Therefore, these old stellar remnants contain valuable information on the stellar evolution theory, the kinematics, and the star formation history of our Galaxy, and the ultimate fate of planetary systems (see [Winget & Kepler 2008](#); [Althaus et al. 2010](#); [García-Berro & Oswalt 2016](#); [Córscico et al. 2019a](#), for reviews). Furthermore, given the large densities that characterize the white dwarf interiors, these compact objects are considered reliable cosmic laboratories to study the properties of baryonic matter under extreme physical conditions ([Isern et al. 2022](#)). Of all the white dwarfs, of special interest are the so-called ultra-massive white dwarfs, which are defined as those with masses larger than $\sim 1.05 M_{\odot}$. Ultra-massive white dwarfs play a key role in constraining the threshold above which stars explode as super-

nova to create neutron stars, and they are involved in extreme astrophysical phenomena such as type Ia supernovae, micronevadae explosions, radio transients via an accretion-induced collapse ([Moriya 2019](#)), as well as stellar mergers. Ultra-massive white dwarfs are also powerful tools to study the theory of high-density plasmas and general relativity.

The theoretical evolution of ultra-massive white dwarfs with masses up to 1.29 M_{\odot} was studied in detail in [Camisassa et al. \(2019, 2022\)](#). These studies provide white dwarf evolutionary sequences with a oxygen-neon (ONe) and carbon-oxygen (CO) core-chemical composition, considering realistic initial chemical profiles that are the result of the full progenitor evolution calculated in [Siess \(2010\)](#) and [Althaus et al. \(2021\)](#), respectively. This set of ultra-massive white dwarf evolutionary models provides an appropriate tool to study the ultra-massive white dwarf population in our Galaxy, subject to the condition that white dwarf masses do not exceed 1.29 M_{\odot} .

In recent years, observations of ultra-massive white dwarfs have been reported in several studies ([Mukadam et al. 2004](#);

[★] The cooling sequences are publicly available at <http://evolgroup.fcaglp.unlp.edu.ar/TRACKS/tracks.html>

Nitta et al. 2016; Gianninas et al. 2011; Kleinman et al. 2013; Bours et al. 2015; Kepler et al. 2016; Curd et al. 2017; Kilic et al. 2021; Hollands et al. 2020; Caiazzo et al. 2021; Torres et al. 2022). In particular, Gagné et al. (2018) derived a mass of $1.28 \pm 0.08 M_{\odot}$ for the long-known white dwarf GD 50. The number of ultra-massive white dwarfs with mass determinations beyond $1.29 M_{\odot}$ is steadily increasing with current observations. Pshirkov et al. (2020) discovered a rapidly rotating ultra-massive white dwarf, WD J183202.83+085636.24, with $M = 1.33 \pm 0.01 M_{\odot}$; meanwhile, Caiazzo et al. (2021) reported the existence of a highly magnetized, rapidly rotating ultra-massive white dwarf, ZTF J190132.9+145808.7, with a mass of $\sim 1.327\text{--}1.365 M_{\odot}$. Kilic et al. (2021) studied the most massive white dwarfs in the solar neighborhood and concluded that other 22 white dwarfs could also have masses over $1.29 M_{\odot}$, if they had pure H envelopes and CO cores. Furthermore, Scholz (2022) confirms the existence of a branch of faint blue white dwarfs in the *Gaia* color magnitude diagram, with some of them also reported in Kilic et al. (2020), which is mainly composed of ultra-massive white dwarfs more massive than $1.29 M_{\odot}$.

In addition to all these observations, gravity(*g*)-mode pulsations have been detected in at least four ultra-massive white dwarfs (Kanaan et al. 1992; Hermes et al. 2013; Curd et al. 2017; Rowan et al. 2019). Although these stars have masses slightly below $1.29 M_{\odot}$, we expect more massive pulsating white dwarfs to be identified in the coming years with the advent of huge volumes of high-quality photometric data collected by space missions such as the ongoing TESS mission (Ricker et al. 2015) and the *Cheops* (Moya et al. 2018) mission, as well as the future *Plato* space telescope (Piotto 2018). This high volume of photometric data is expected to make asteroseismology a promising tool to study the structure and chemical composition of ultra-massive white dwarfs (De Gerónimo et al. 2019; Córscico et al. 2019b). In fact, several successful asteroseismological analyses of white dwarfs have been carried out using space data thanks to the *Kepler/K2* mission (Borucki et al. 2010; Howell et al. 2014; Córscico 2020) and TESS (Córscico 2022).

The increasing number of detected ultra-massive white dwarfs with masses beyond $1.29 M_{\odot}$ as well as the immediate prospect of detecting pulsating white dwarfs with such masses, demand new appropriate theoretical evolutionary models to analyze them. Recently, Schwab (2021a) has studied the evolution of white dwarfs more massive than $1.29 M_{\odot}$ with the focus on neutrino cooling via the Urca process, showing that this process is important for the age determination of ONe-core white dwarf stars. These models were calculated employing the set of standard equations to solve the stellar structure and evolution under the assumption of Newtonian gravity. However, the importance of general relativity for the structure of the most massive white dwarfs cannot be completely disregarded. This was recently assessed by Carvalho et al. (2018), who solved the general relativistic hydrostatic equilibrium equation for a completely degenerate ideal Fermi electron gas. They demonstrate that for fixed values of total mass, large deviations (up to 50%) in the Newtonian white dwarf radius are expected compared to the general relativistic white dwarf radius. The impact of a non-ideal treatment of the electron gas on the equilibrium structure of relativistic white dwarfs was studied by Rotondo et al. (2011) and Mathew & Nandy (2017), who derived the mass-radius relations and critical masses in the general relativity framework for white dwarfs of different core chemical compositions. These studies conclude that general relativistic effects are relevant for the determination of the radius of massive white dwarfs. de Carvalho et al. (2014) and, more recently, Nunes et al. (2021)

investigated the general relativity effects in static white dwarf structures of nonideal matter in the case of finite temperature. While de Carvalho et al. (2014) focused their work on the effects of finite temperature on extremely low-mass white dwarfs, Nunes et al. (2021) studied the stability of massive hot white dwarfs against radial oscillations, inverse β -decay, and pycnonuclear reactions. They find that the effect of the temperature is still important for determining the radius of very massive white dwarfs.

Despite several works devoted to the study of the effects of general relativity on the structure of white dwarfs, none have calculated the evolution of such structures. Moreover, in all of the works mentioned above, the white dwarf models are assumed to be composed solely of one chemical element. The exact chemical composition determines both the mass limit of white dwarfs and the nature of the instability (due to general-relativity effects or to β -decays; e.g., Rotondo et al. 2011). In this work, we computed the first set of constant rest-mass ultra-massive ONe white dwarf evolutionary models that fully take into account the effects of general relativity on their structural and evolutionary properties. Furthermore, we considered realistic initial chemical profiles as predicted by the progenitor evolutionary history. We employed the La Plata stellar evolution code, LPCODE, to compute the full evolutionary sequence of 1.29 , 1.31 , 1.33 , 1.35 , and $1.369 M_{\odot}$ white dwarfs. The standard equations of stellar structure and evolution solved in this code have been modified to include the effects of general relativity. For comparison purposes, the same sequences have been computed for the Newtonian gravity case. We assessed the resulting cooling times and provide precise time dependent mass-radius relations for relativistic ultra-massive white dwarfs. We also provide magnitudes in *Gaia*, the Sloan Digital Sky Survey, and Pan-STARRS passbands, using the model atmospheres of Koester (2010), Koester & Kepler (2019). This set of cooling sequences, together with the models calculated in Camisassa et al. (2019, 2022), provide a solid theoretical framework to study the most massive white dwarfs in our Galaxy.

This paper is organized as follows. In Sect. 2 we describe the modifications to our code to incorporate the effects of general relativity. In Sect. 3 we detail the main constitutive physics of our white dwarf sequences. Section 4 is devoted to the impact of general relativity effects on the relevant evolutionary properties of our massive white dwarfs. In this section we also compare and discuss the predictions of our new white dwarf sequences with observational data of ultra-massive white dwarfs, in particular with the recently reported faint blue branch of ultra-cool and ultra-massive objects revealed by the *Gaia* space mission. Finally, in Sect. 5 we summarize the main findings of this work.

2. Equations of stellar structure and evolution in general relativity

Our set of ultra-massive ONe white dwarf evolutionary sequences was computed with the stellar evolution code LPCODE developed by La Plata group, which has been widely used and tested in numerous stellar evolution contexts of low-mass stars and particularly in white dwarf stars (Althaus et al. 2003, 2005, 2015; Salaris et al. 2013; Miller Bertolami 2016; Silva Aguirre et al. 2020; Christensen-Dalsgaard et al. 2020). For this work, the stellar structure and evolution equations were modified to include the effects of general relativity, following the formalism given in Thorne (1977). Within this formalism, the fully general relativistic partial differential equations governing the evolution of a spherically symmetric star are presented

in a way that they resemble the standard Newtonian equations of stellar structure (Kippenhahn et al. 2012). Specifically, the structure and evolution of the star is specified by the Tolman-Oppenheimer-Volkoff (TOV) equation of hydrostatic equilibrium, the equation of mass distribution, the luminosity equation, and the energy transport equation:

$$\frac{\partial P}{\partial m} = -\frac{Gm}{4\pi r^4} \mathcal{H} \mathcal{G} \mathcal{V}, \quad (1)$$

$$\frac{\partial r}{\partial m} = (4\pi r^2 \varrho \mathcal{V})^{-1}, \quad (2)$$

$$\frac{1}{\mathcal{R}^2} \frac{\partial(L\mathcal{R}^2)}{\partial m} = -\varepsilon_v - \frac{1}{\mathcal{R}} \frac{\partial u}{\partial t} + \frac{1}{\mathcal{R}} \frac{P}{\varrho^2} \frac{\partial \varrho}{\partial t}, \quad (3)$$

$$\frac{\partial(T\mathcal{R})}{\partial m} = -\frac{3}{64\pi^2 ac} \frac{\kappa L}{r^4 T^3} \mathcal{R} \quad \text{if } \nabla_{\text{rad}} \leq \nabla_{\text{ad}}, \quad (4)$$

$$\frac{\partial \ln T}{\partial m} = \nabla \frac{\partial \ln P}{\partial m} \quad \text{if } \nabla_{\text{rad}} > \nabla_{\text{ad}}, \quad (5)$$

where t is the Schwarzschild time coordinate, m is the rest mass inside a radius r or baryonic mass, that is, the mass of one hydrogen atom in its ground state multiplied by the total number of baryons inside r , and ϱ is the density of rest mass. Throughout the cooling process, the total baryonic mass remains constant. c is the speed of light, u is the internal energy per unit mass, and ε_v is the energy lost by neutrino emission per unit mass; \mathcal{H} , \mathcal{G} , \mathcal{V} , and \mathcal{R} are the dimensionless general relativistic correction factors, which turn to unity in the Newtonian limit. These factors correspond, respectively, to the enthalpy, gravitational acceleration, volume, and redshift correction factors and are given by

$$\mathcal{H} = \frac{\varrho^t}{\varrho} + \frac{P}{\varrho c^2}, \quad (6)$$

$$\mathcal{G} = \frac{m^t + 4\pi r^3 P/c^2}{m}, \quad (7)$$

$$\mathcal{V} = \left(1 - \frac{2Gm^t}{rc^2}\right)^{-1/2}, \quad (8)$$

$$\mathcal{R} = e^{\Phi/c^2}, \quad (9)$$

where m^t is the mass-energy inside a radius r and includes contributions from the rest-mass energy, the internal energy, and the gravitational potential energy, which is negative. ϱ^t is the density of total nongravitational mass-energy, and includes the density of rest mass plus contributions from kinetic and potential energy density due to particle interactions (it does not include the gravitational potential energy density), that is, $\varrho^t = \varrho + (u\varrho)/c^2$. Since the internal and gravitational potential energy change during the course of evolution, the stellar mass-energy is not a conserved quantity. Φ is the general relativistic gravitational potential related to the temporal metric coefficient. At variance with the Newtonian case, the gravitational potential appears explicitly in the evolution equations. We note that the TOV hydrostatic equilibrium equation differs markedly from its Newtonian counterpart, providing a steeper pressure gradient. We also note that the presence of \mathcal{V} in that equation prevents m^t from being larger than $rc^2/2G$.

The radiative gradient ∇_{rad} is given by

$$\nabla_{\text{rad}} = \frac{3}{16\pi acG} \frac{\kappa LP}{mT^4} \frac{1}{\mathcal{H} \mathcal{G} \mathcal{V}} + \left(1 - \frac{\varrho^t/\varrho}{\mathcal{H}}\right). \quad (10)$$

In Eq. (5), ∇ is the convective temperature gradient, which, in the present work, is given by the solution of the mixing length

theory. In ultra-massive white dwarfs, the occurrence of convection is restricted to a very narrow outer layer¹, which is mostly adiabatic. We followed Thorne (1977) in generalizing the mixing length theory to general relativity. In Eq. (3), we omit the energy generation by nuclear reactions since these are not happening in our models. However, they should be added when taking Urca processes into account.

To solve Eqs. (1)–(5) we need two additional equations that relate m^t and Φ with m . These two equations, which are not required in the Newtonian case, have to be solved simultaneously with Eqs. (1)–(5). These extra equations are given by (see Thorne 1977)

$$\frac{\partial m^t}{\partial m} = \frac{\varrho^t}{\varrho} \frac{1}{\mathcal{V}}, \quad (11)$$

$$\frac{\partial \Phi}{\partial m} = \frac{Gm}{4\pi r^4 \varrho} \mathcal{G} \mathcal{V}. \quad (12)$$

For the boundary conditions, we proceeded as follows. The rest mass, total mass-energy, and radius of the star correspond, respectively, to the values of m , m^t , and r at the surface of the star. We denote them as

$$M_{\text{WD}} = m, \quad M_{\text{G}} = m^t, \quad R = r \quad \text{at the surface.} \quad (13)$$

M_{G} is the total gravitational mass, that is, the stellar mass that would be measured by a distant observer, which turns out to be less than the total baryonic mass of the white dwarf. Outer boundary conditions for our evolving models are provided by the integration of

$$\frac{dP}{d\tau} = \frac{g^t}{\kappa}, \quad (14)$$

and assuming a gray model atmosphere. τ is the optical depth and g^t is the “proper” surface gravity of the star (as measured on the surface) corrected by general relativistic effects and given by

$$g^t = \frac{GM_{\text{G}}}{R^2} \mathcal{V}. \quad (15)$$

In addition, the general relativistic metric for space time in the star interior must match to the metric outside created by the star (Schwarzschild metric). The match requires that Φ satisfies the following surface boundary condition:

$$\Phi = \frac{1}{2} c^2 \ln \left(1 - \frac{2GM_{\text{G}}}{Rc^2}\right) \quad \text{at } m = M_{\text{WD}}. \quad (16)$$

At the stellar center, $m = 0$, we have $m^t = 0$, $r = 0$, and $L = 0$.

3. Initial models and input physics

We computed the full evolution of 1.29, 1.31, 1.33, 1.35, and 1.369 M_{\odot} white dwarfs assuming the same ONE core abundance distribution for all of them. The adopted core composition corresponds to that of the 1.29 M_{\odot} hydrogen-rich white dwarf sequence considered in Camisassa et al. (2019), which has been derived from the evolutionary history of a 10.5 M_{\odot} progenitor star (Siess 2010). In this work, we restricted ourselves to ONE-core massive white dwarfs, thus extending the range of ONE

¹ This may not be true if neutrino cooling via the Urca process is considered, in which case an inner convection zone is expected; see Schwab (2021a).

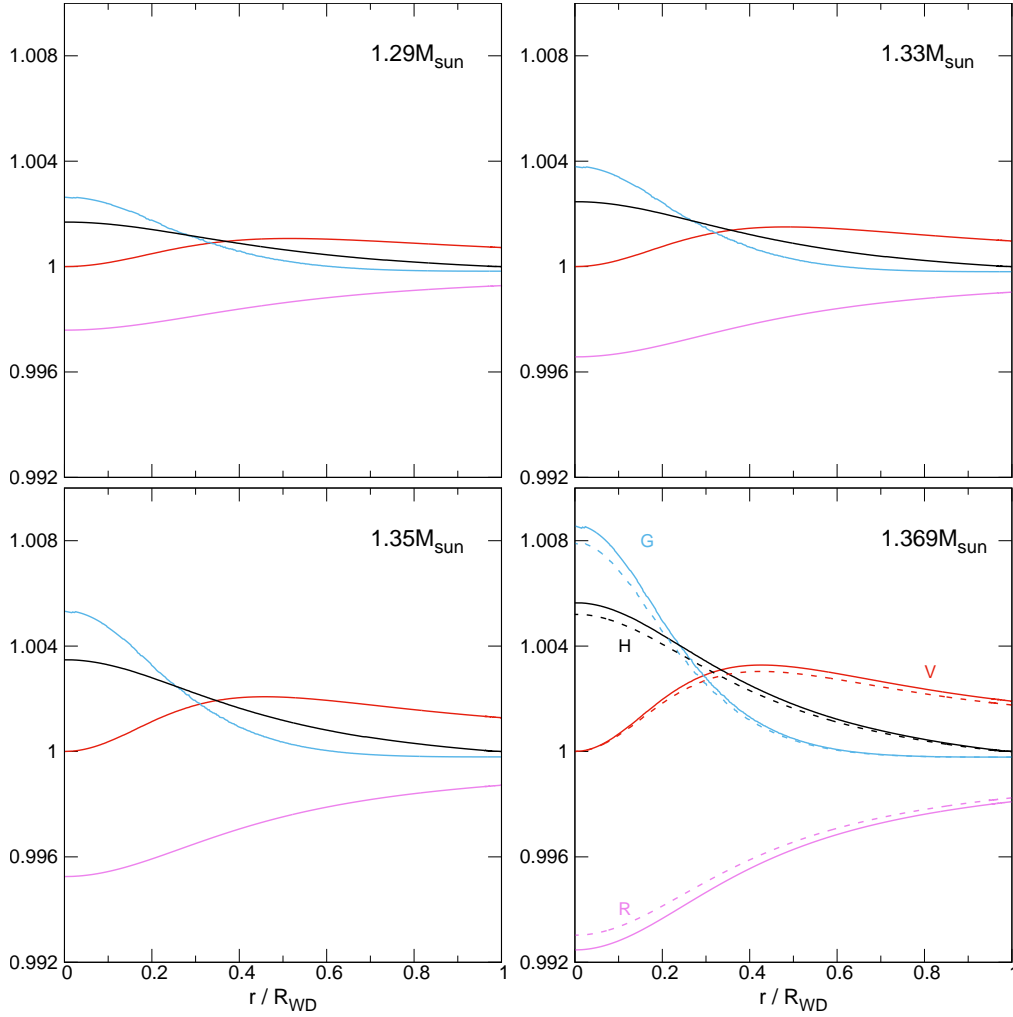


Fig. 1. Run of general relativistic correction factors \mathcal{H} , \mathcal{G} , \mathcal{V} , and \mathcal{R} (black, blue, red, and pink lines, respectively) for 1.29, 1.33, 1.35, and $1.369 M_{\odot}$ white dwarf models at $\log L/L_{\odot} = -3$ in terms of the fractional radius. Dashed lines in the bottom right panel illustrate the behavior of the same factors for a $1.369 M_{\odot}$ model at $\log L/L_{\odot} = -0.4$.

white dwarf sequences already computed in Camisassa et al. (2019) within the framework of the Newtonian theory of stellar interior. One core white dwarfs are expected as a result of semi-degenerate carbon burning during the single evolution of progenitor stars that evolve to the super asymptotic giant branch (García-Berro et al. 1997; Gil-Pons et al. 2005; Siess 2006; Doherty et al. 2010; Ventura & D’Antona 2011). Recent calculations of the remnant of a double white dwarf merger also predict ONe core composition as a result of off-center carbon burning in the merged remnant when the remnant mass is larger than $1.05 M_{\odot}$ (see Schwab 2021b). In particular, it is thought that a considerable fraction of the massive white dwarf population is formed as a result of stellar mergers (Temminck et al. 2020; Cheng et al. 2020; Torres et al. 2022). We note, however, that the existence of ultra-massive white dwarfs with CO cores resulting from single evolution cannot be discarded (see Althaus et al. 2021; Wu et al. 2022).

The adopted input physics for our relativistic white dwarf models is the same as that in Camisassa et al. (2019). In brief, the equation of state for the low-density regime is that of Magni & Mazzitelli (1979), and that of Segretain et al. (1994) was used for the high-density regime, which takes into account all the important contributions for both the solid and liquid phases. We include neutrino emission for pair, photo, and Bremsstrahlung

processes using the rates of Itoh et al. (1996), and those of Haft et al. (1994) for plasma processes. The energetics resulting from crystallization processes in the core was included as in Camisassa et al. (2019), and it is based on the two-component phase diagram of dense ONe mixtures appropriate for massive white dwarf interiors, Medin & Cumming (2010). As shown by Blouin & Daligault (2021), ^{23}Na and ^{24}Mg impurities only have a negligible impact on the ONe phase diagram, and the two-component ONe phase diagram can be safely used to assess the energetics resulting from crystallization. We did not consider the energy released by a ^{22}Ne sedimentation process, since it is negligible in ONe white dwarfs (Camisassa et al. 2021).

4. General relativity effects on the evolution of massive white dwarfs

Here, we describe the impact of general relativity effects on the relevant properties of our constant rest-mass evolutionary tracks. We begin by examining Fig. 1, which displays the general relativistic correction factors \mathcal{H} , \mathcal{G} , \mathcal{V} , and \mathcal{R} (black, blue, red, and pink lines, respectively) in terms of the fractional radius for the 1.29, 1.33, 1.35, and $1.369 M_{\odot}$ white dwarf models at $\log L/L_{\odot} = -3$. Dashed lines in the bottom right panel illustrate the run of the same factors for a $1.369 M_{\odot}$ white dwarf model at

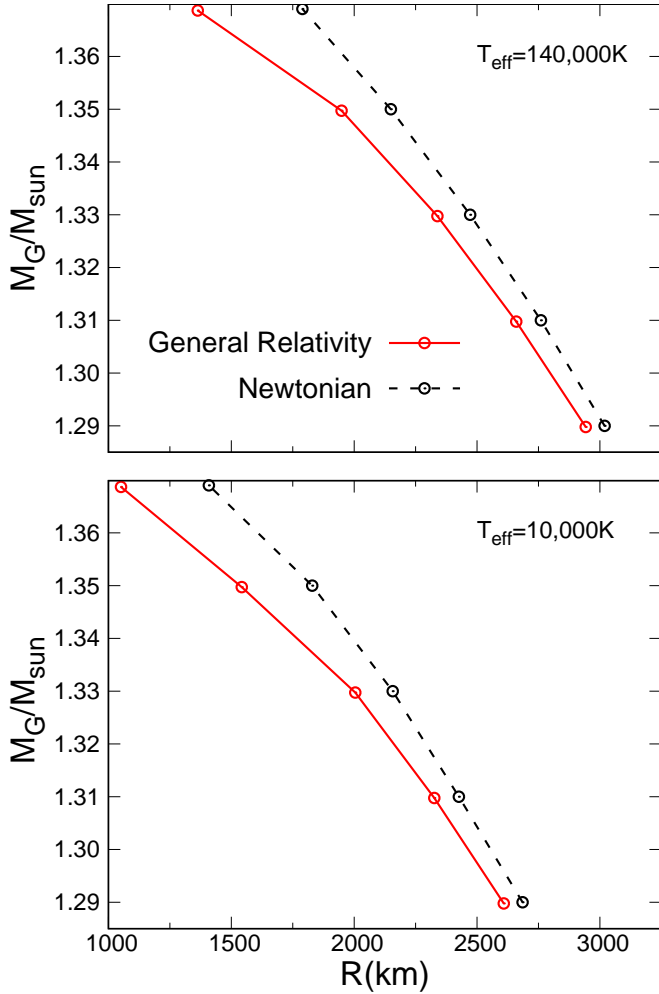


Fig. 2. Gravitational mass versus stellar radius for our ONE ultra-massive white dwarf models considering (red symbols and lines) and disregarding (black symbols and lines) the effects of general relativity at two different effective temperatures.

$L/L_{\odot} = -0.4$ ($\log T_{\text{eff}} = 5$). We recall that these factors are unity in the Newtonian limit. As expected, the importance of general relativistic effects increases as the stellar mass is increased. We note that \mathcal{V} is unity at the center and attains a maximum value at some inner point in the star. The relativistic factor \mathcal{R} decreases toward the center, departing even more from unity; meanwhile, the other factors, \mathcal{G} and \mathcal{H} , increase toward the center of the star. The behavior of the relativistic correction factors can be traced back to curvature effects, as well as to the fact that the pressure and the internal energy appear as a source for gravity in general relativity. For maintaining hydrostatic equilibrium, then, both density and pressure gradients are steeper than in Newtonian gravity. This makes the factors \mathcal{G} and \mathcal{H} , which depend directly on density and pressure, to increase towards the center of the star. The relativistic factor \mathcal{V} , which can be interpreted as a correction to the volume, would be unity at the center of the star where the volume is zero and increase because of the increasing density in general relativity respect to the density in Newtonian gravity. However, as the departures from the Newtonian case decrease toward the surface of the star, \mathcal{V} decreases toward the outside, achieving a maximum value in between. We note that the relativistic factors depend slightly on the effective temperature.

The impact of relativistic effects on the mass-radius relation at two different effective temperatures can be appreciated in Fig. 2. We note that for the most massive white dwarfs, at a given gravitational mass, the radius is markedly smaller in the case that the general relativity effects are taken into account. At a stellar mass of $1.369 M_{\odot}$ the stellar radius becomes only 1050 km, 25% smaller than predicted by the Newtonian treatment (see Table 1). As in the Newtonian case, the effect of finite temperature on the stellar radius is still relevant in very massive white dwarfs. We mention that general relativistic corrections become negligible for stellar masses smaller than $\approx 1.29 M_{\odot}$. In particular, for stellar masses below that value, the stellar radius results below 2% smaller when general relativity effects are taken into account.

In our calculations, ONE white dwarfs more massive than $1.369 M_{\odot}$ become gravitationally unstable (which occurs at a given finite central density) with respect to general relativity effects, in agreement with the findings for zero-temperature models reported in Rotondo et al. (2011) for a pure-oxygen white dwarf ($1.38024 M_{\odot}$) and Mathew & Nandy (2017) for white dwarfs composed of oxygen ($1.3849 M_{\odot}$) or of neon ($1.3788 M_{\odot}$), although their values are slightly higher². We mention that for the $1.369 M_{\odot}$ white dwarf model, the central density in the general relativity case reaches $2.11 \times 10^{10} \text{ g cm}^{-3}$ (see Table 1). Such density is near the density threshold for inverse β -decays. We have not considered that matter inside our white dwarf models may experience instability against the inverse β -decay. O or Ne white dwarfs are expected to become unstable against the inverse β -decay process at a stellar mass near the critical mass resulting from general relativity effects, on the order of $1.37 M_{\odot}$ (see Rotondo et al. 2011; Mathew & Nandy 2017).

The inner profile of rest mass and density of rest mass for the $1.369 M_{\odot}$ white dwarf model in the general relativity and Newtonian cases are shown in the upper and bottom panels of Fig. 3, respectively. For such a massive white dwarf model, general relativity effects strongly alter the stellar structure, causing matter to be much more concentrated toward the center of the star and the central density to be larger than in the Newtonian case. The impact remains noticeable toward lower stellar masses, although to a lesser extent, as can be noted for the case of the $1.35 M_{\odot}$ white dwarf model shown in the bottom panel of Fig. 3 (dotted lines). In view of this, the run of the gravitational field versus radial coordinate for the general relativity case differs markedly from that resulting from the Newtonian case. This is shown in Fig. 4 for the $1.369 M_{\odot}$, $1.35 M_{\odot}$, and $1.29 M_{\odot}$ white dwarf models. In particular, the gravitational field in the general relativistic case as measured far from the star is given by

$$g^{\text{GR}} = \frac{Gm}{r^2} \mathcal{G} \mathcal{V}^2. \quad (17)$$

Clearly, the gravitational field in the most massive of our models is strongly affected by general relativity. In the stellar interior, large differences arise in the gravitational field due to the inclusion of general relativity effects. We note that such differences do not arise from the relativistic correction factors $\mathcal{G} \mathcal{V}^2$ (see Fig. 1) to the Newtonian gravitational field $g^{\text{New}} = Gm/r^2$ that appear explicitly in Eq. (17), but from the solution of the relativistic equilibrium instead, which gives a different run for $m(r)$ compared to the Newtonian case.

Additionally, the surface gravity and stellar radius are affected by the effects of general relativity. These quantities are shown in Fig. 5 in terms of the effective temperature for all of

² Preliminary computations we performed for oxygen-rich core white dwarfs show that they become unstable at $1.382 M_{\odot}$.

Table 1. Relevant characteristics of our sequences at $T_{\text{eff}} = 10\,000\text{ K}$.

M_{WD} (M_{\odot})	M_{G} (M_{\odot})	R^{Newt} (km)	R^{GR} (km)	$\log g^{\text{Newt}}$ (cm s^{-2})	$\log g^{\text{GR}}$ (cm s^{-2})	$\rho_{\text{c}}^{\text{Newt}}$ (g cm^{-3})	$\rho_{\text{c}}^{\text{GR}}$ (g cm^{-3})
1.29	1.28977	2685.40	2608.86	9.375	9.401	6.71×10^8	7.51×10^8
1.31	1.30976	2426.04	2326.17	9.470	9.507	9.98×10^8	1.17×10^9
1.33	1.32974	2156.90	2004.60	9.579	9.643	1.57×10^9	2.06×10^9
1.35	1.34972	1829.29	1542.51	9.728	9.878	2.90×10^9	5.36×10^9
1.369	1.36871	1408.77	1051.16	9.961	10.217	7.42×10^9	2.11×10^{10}

Notes. M_{WD} : total baryonic mass. M_{G} : total gravitational mass. R^{Newt} : stellar radius in the Newtonian case. R^{GR} : stellar radius in the general relativity case. g^{Newt} : surface gravity in the Newtonian case. g^{GR} : surface gravity in the general relativity case. $\rho_{\text{c}}^{\text{Newt}}$: central density of rest mass in the Newtonian case. $\rho_{\text{c}}^{\text{GR}}$: central density of rest mass in the general relativity case.

our sequences for the general relativity and Newtonian cases, using solid and dashed lines, respectively. In the most massive sequences, general relativity effects markedly alter the surface gravity and stellar radius. In this sense, we infer that general relativity effects lead to a stellar mass value about $0.015 M_{\odot}$ smaller for cool white dwarfs with measured surface gravities of $\log g \approx 10$. The photometric measurements of Kilic et al. (2021) for the radius of the ultra-massive white dwarfs in the solar neighborhood are also plotted in this figure. For the more massive of such white dwarfs, the stellar radius results 2.8–4% smaller when general relativity effects are taken into account.

We note that most of our sequences display a sudden increase in their surface gravity at high effective temperatures. As noted in Camisassa et al. (2019), this is related to the onset of core crystallization (marked with blue filled circles in each sequence depicted in Fig. 5), which modifies the distribution of ^{16}O and ^{20}Ne . Specifically, the abundance of ^{20}Ne increases in the core of the white dwarf as crystallization proceeds, leading to larger Coulomb interactions and hence to denser cores, and, therefore, to higher surface gravities. This behavior can also be regarded as a sudden radius decrease (bottom panel of Fig. 5). In this context, we note that the density increase due to the increase in the core abundance of ^{20}Ne during crystallization eventually causes ONe white dwarf models with stellar masses larger than $\gtrsim 1.36 M_{\odot}$ to become gravitationally unstable against general relativity effects. In order to explore the mass range of stable white dwarfs in the absence of this processes, the $1.369 M_{\odot}$ relativistic sequence was computed disregarding the effect of phase separation (but not latent heat) during crystallization.

4.1. General relativity effects on the white dwarf cooling times

The cooling properties of the ultra-massive white dwarfs are also markedly altered by general relativity effects, in particular the the most massive ones. This is illustrated in Fig. 6, which compares the cooling times of our models for the general relativity and Newtonian cases, with solid and dashed lines, respectively. The cooling times are set to zero at the beginning of cooling tracks at very high effective temperatures. Gravothermal energy is the main energy source of the white dwarfs, except at very high effective temperatures where energy released during the crystallization process contributes to the budget of the star. As noticed by Camisassa et al. (2021), ultra-massive ONe-core white dwarfs evolve extremely quickly into faint magnitudes. General relativity effects cause ultra-massive white dwarfs to evolve faster than in the Newtonian case at advanced stages of evolution. In particular, the $1.369 M_{\odot}$ relativistic sequence

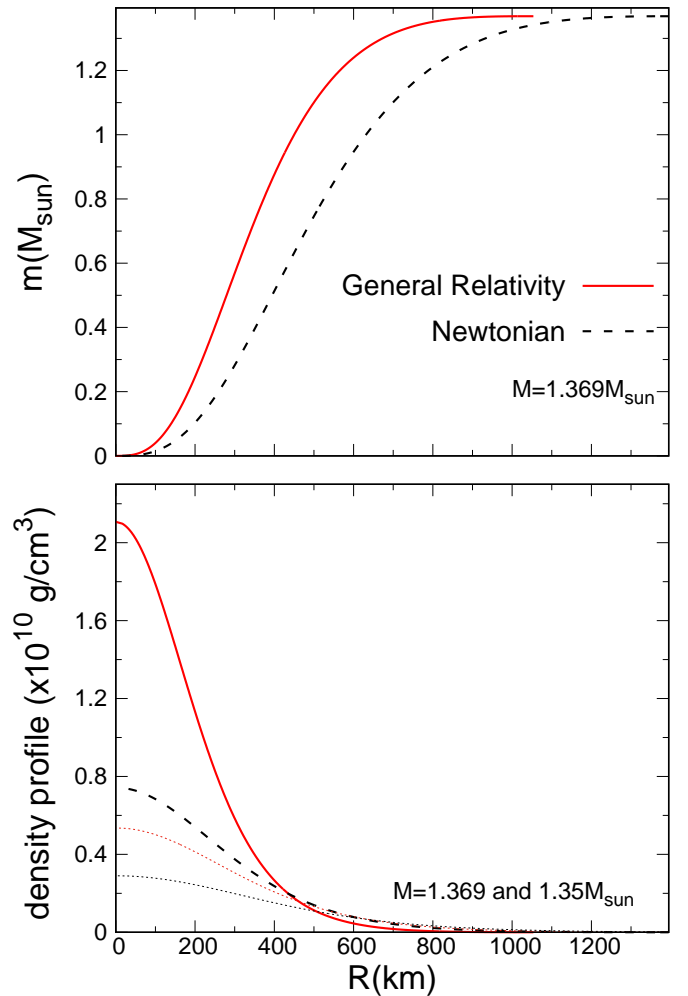


Fig. 3. Rest mass m (upper panel) and density of rest mass (bottom panel) for the general relativity and Newtonian cases (red solid and black dashed lines, respectively) in terms of radial coordinate for $1.369 M_{\odot}$ white dwarf models at advanced stage of evolution. Dotted lines in the bottom panel depict the situation for the $1.35 M_{\odot}$ models.

reaches $\log(L/L_{\odot}) = -4.5$ in only ~ 0.5 Gyr, in contrast with the ~ 0.9 Gyr needed in the Newtonian case. The larger internal densities inflicted by general relativity make the Debye cooling phase more relevant than in the Newtonian case at a given stellar mass, thus resulting in a faster cooling for the sequences that include general relativity effects. The fast cooling of these objects, together with their low luminosity and rare formation

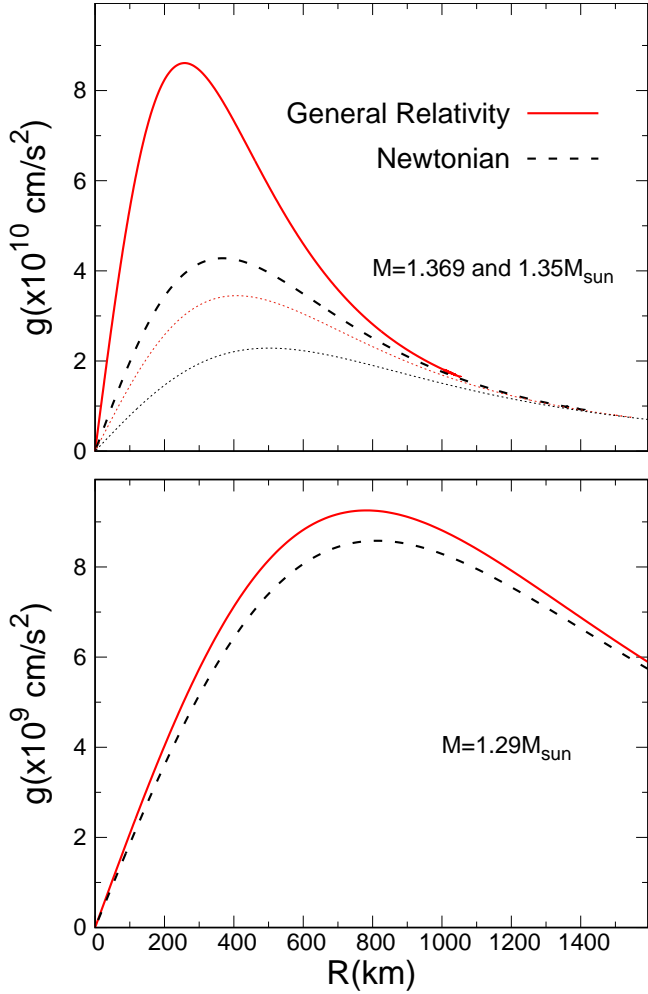


Fig. 4. General relativity and Newtonian gravitational field (red solid and black dashed lines, respectively) versus radial coordinate for the $1.369 M_{\odot}$ and $1.29 M_{\odot}$ white dwarf models at an advanced stage of evolution. Dotted lines in the *upper panel* depict the situation for the $1.35 M_{\odot}$ models.

rates, would make them hard to observe. The trend in the cooling behavior is reversed at earlier stages of evolution, where white dwarfs computed in the general relativity case evolve more slowly than their Newtonian counterparts. This is because white dwarfs computed in the general relativity case crystallize at higher luminosities (because of their larger central densities), with the consequent increase in the cooling times at those stages. In the $1.369 M_{\odot}$ relativistic sequence, the full impact of crystallization on the cooling times is smaller due to the fact that we neglected the process of phase separation during crystallization in that sequence.

We mention that we neglected the neutrino emission resulting from Urca process, which is relevant in ONe white dwarfs at densities in excess of 10^9 g cm^{-3} (Schwab 2021a). In our modeling, such densities are attained at models with stellar masses of $\geq 1.33 M_{\odot}$ (see Table 1). Hence, the depicted cooling times for the sequences with stellar masses above this value may be overestimated at high and intermediate luminosities. A first attempt to include the Urca cooling process from a ^{23}Na – ^{23}Ne Urca pair in our stellar code leads to the formation of a mixing region below the Urca shell, as reported by Schwab (2021a). Because of the temperature inversion caused by Urca process, our most massive white dwarf models develop off-centered crystalliza-

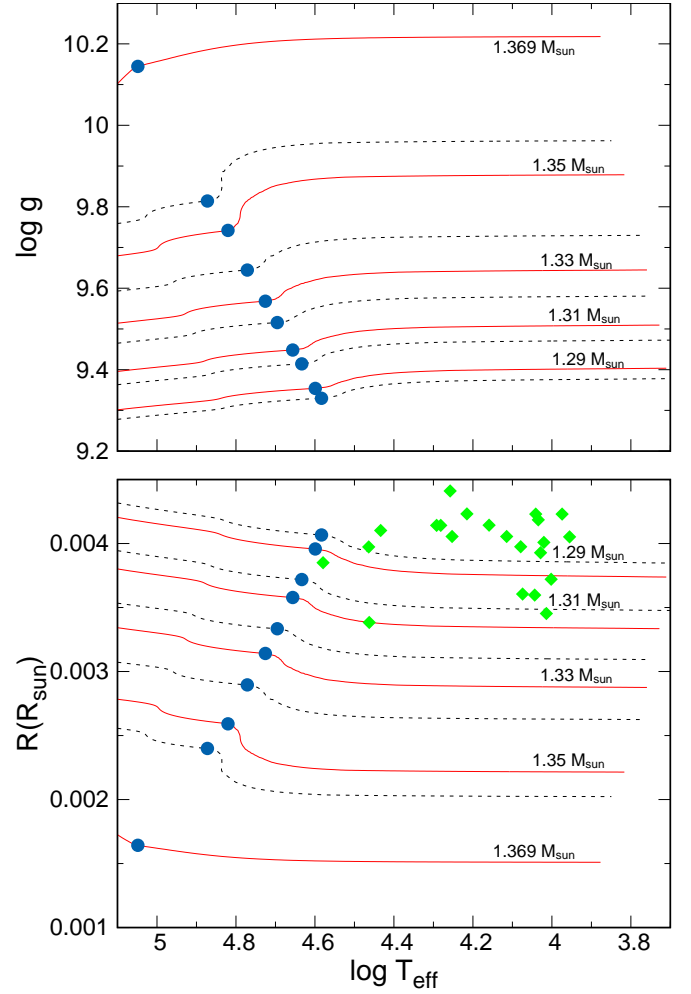


Fig. 5. Surface gravity and stellar radius (in solar units) in terms of effective temperature for all of our sequences are displayed in the *upper* and *bottom panels*, respectively. Red solid and black dotted lines correspond to the general relativity and Newtonian cases, respectively. From *bottom (top)* to *top (bottom)*, curves in the *upper (bottom)* panel correspond to 1.29 , 1.31 , 1.33 , 1.35 , and $1.369 M_{\odot}$ white dwarf cooling sequences. Blue filled circles denote the onset of core crystallization in each sequence. The most massive white dwarfs in the solar neighborhood analyzed in Kilic et al. (2021) are displayed using green filled diamonds.

tion. We find numerical difficulties in modeling the interaction of crystallization and the Urca process-induced mixing that prevent a consistent computation of white dwarf cooling during these stages. As recently shown by Schwab (2021a), the cooling of such massive white dwarfs is dominated by neutrino cooling via the Urca process during the first 100 Myr after formation. Our focus in this work is on the effects of general relativity on ultra-massive white dwarfs, so we leave the difficult treatment of Urca-process impacts on the structure of relativistic white dwarfs for an upcoming work.

4.2. Observational constraints on ultra-massive white dwarf models

The ESA *Gaia* mission has provided an unprecedented wealth of information about stars (see Gaia Collaboration 2021a, and references therein). In particular, nearly $\approx 359\,000$ white dwarf candidates have been detected (Gentile Fusillo et al. 2021), with

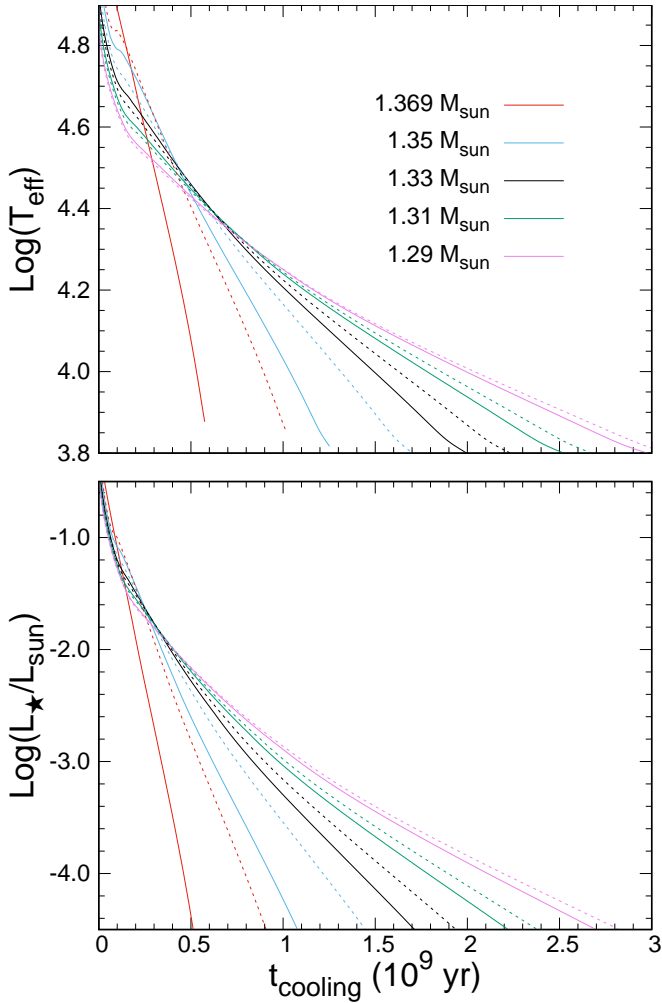


Fig. 6. Effective temperature and surface luminosity (*upper and bottom panels*) versus the cooling times for our 1.29, 1.31, 1.33, 1.35, and 1.369 M_{\odot} white dwarf sequences. Solid (dashed) lines correspond to the general relativity (Newtonian) cases. Cooling time is counted from the time of white dwarf formation.

it being estimated that the sample up to 100 pc from the Sun can practically be considered complete (Jiménez-Esteban et al. 2018). The extreme precision of astrometric and photometric measures allow us to derive accurate color-magnitude diagrams with which to test our models. Some unexpected peculiar features have already been observed in the *Gaia* white dwarf color-magnitude diagram (Gaia Collaboration 2018), for instance the Q branch, resulting from crystallization and sedimentation delays (Cheng et al. 2019; Tremblay et al. 2019; Camisassa et al. 2021). However, a new branch called the faint blue branch has been reported by Scholz (2022). This faint blue branch is formed by ~ 60 ultra-cool and ultra-massive objects, which have been astrometrically and photometrically verified and cross-validated with the *Gaia* catalog of nearby stars (Gaia Collaboration 2021b) and the white dwarf catalog of Gentile Fusillo et al. (2021). It is also important to mention that some of these objects that form this peculiar feature in the color-magnitude diagram have already been reported, see Kilic et al. (2020) and references therein. Most of these white dwarfs exhibit a near-infrared flux deficit that has been attributed to the effects of molecular collision-induced absorption in mixed hydrogen-helium atmospheres, Bergeron et al. (2022). Some

issues still remain to be clarified under this assumption and not all the objects in Scholz (2022) are present in the analysis of Bergeron et al. (2022). Consequently, for our purpose here, which is not in contradiction with the analysis of Bergeron et al. (2022), we adopted hydrogen-pure atmosphere models for the analysis of the entire Scholz (2022) sample, where particular objects are treated individually.

In the left panel of Fig. 7, we show a color-magnitude diagram for the 100 pc white dwarf *Gaia* EDR3 population (gray dots) together with the faint blue branch objects from Scholz (2022; solid red circles). The color-magnitude diagram selected is absolute magnitude G versus $G_{BP}-G$, instead of $G_{BP}-G_{RP}$, thus minimizing the larger errors induced by the G_{RP} filter for faint objects. We also provide the magnitudes for our relativistic and Newtonian models (black and cyan lines, respectively) in *Gaia* EDR3 passbands (DR2, Sloan Digital Sky Survey, Pan-STARRS and other passbands are also available upon request) using the non-gray model atmospheres of Koester (2010) and Koester & Kepler (2019). Isochrones of 0.25, 0.5, 1, and 2 Gyr for our relativistic model are also shown (dashed black line) in Fig. 7. An initial inspection of the *Gaia* color-magnitude diagram reveals that our new white dwarf sequences are consistent with most of the ultra-massive white dwarfs within 100 pc of the Sun. In addition, the relativistic white dwarf sequences are fainter than Newtonian sequences with the same mass. Therefore, general relativity effects must be carefully taken into account when determining the mass and stellar properties of the most massive white dwarfs through *Gaia* photometry. Not considering such effects would lead to an overestimation of their mass and an incorrect estimation of their cooling times. Finally, we check that faint blue branch objects do not follow any particular isochrone, thus ruling out a common temporal origin of these stars.

A closer look at the faint blue branch is depicted in the right panel of Fig. 7. The vast majority of faint blue branch white dwarfs appear to have masses larger than $\sim 1.29 M_{\odot}$. Thus, this sample is ideal for testing our models, and particularly objects that present the largest masses or, equivalently, the smallest radii. Hence, for the analysis presented here and for reasons of completeness we estimated the error bars for objects that lie on the left of the Newtonian 1.369 M_{\odot} track. Errors are propagated from the astrometric and photometric errors provided by *Gaia* EDR3. Although correlations in *Gaia* photometry are very low, we assumed that some correlation may exist between parameters. This way, errors are added linearly and not in quadrature, thus obtaining an upper limit estimate of the error bars. The parameters corresponding to the 20 selected ultra-massive white dwarf candidates of the faint blue branch are presented in Table 2. In the first column we list the *Gaia* EDR3 source ID with a label for an easy identification in Fig. 7. Columns 2 to 5 present the parallax, apparent and absolute G magnitudes, and color $G_{BP}-G$ with their corresponding error, respectively. Columns 6 and 7 represent the observational distance within the color-magnitude diagram measured in σ deviations to the limiting 1.369 M_{\odot} cooling track when the general relativity model or the Newtonian model, respectively, is used. Finally, the last column is a five-digit number flag. The first digit indicates if the relative flux error in the G_{BP} band is larger than or equal to 10% (1) or smaller (0). The second digit indicates if the relative flux error in the G_{RP} band is larger than or equal to 10% (1) or smaller (0). The third digit indicates if the β parameter as defined by Riello et al. (2021) is ≥ 0.1 (1) or < 0.1 (0); if it is 1 then the object is affected by blending. The fourth digit is set to (0) if the renormalized unit vector *ruwe* (Lindegren et al. 2018) is < 1.4

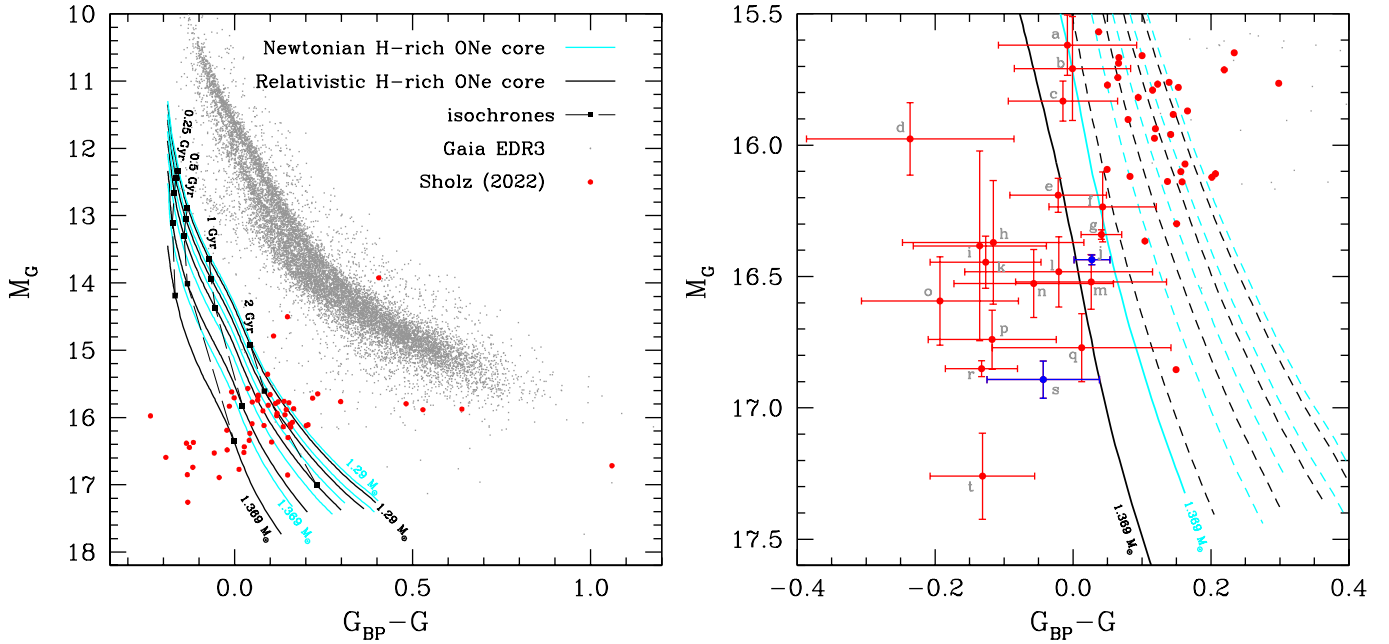


Fig. 7. Theoretical and observational color-magnitude diagrams. *Left panel:* *Gaia* EDR3 color-magnitude diagram. Newtonian and general relativistic cooling sequences are displayed using cyan and black lines, respectively. Their rest masses are, from top to bottom, 1.29, 1.31, 1.33, 1.35, and 1.369 M_{\odot} . The *Gaia* white dwarf population within 100 pc is displayed using gray dots. The faint blue white dwarf branch reported in Scholz (2022) is displayed using large red filled circles. Dashed lines show isochrones of 0.25, 0.5, 1, 2 Gyr. *Right panel:* zoomed-in view of the faint blue white dwarf branch. Objects $\{j, s\}$ (marked in blue) are ideal candidates, compatible at a 1σ level with the general relativistic model but marginally at a 2σ level with Newtonian models.

(indicative that the solution corresponds to a single object) or set to (1) if it is ≥ 1.4 (bad solution or binary system). The fifth digit indicates if the object passes (1) a 5σ cut on the corrected G_{BP} and G_{RP} flux excess or not (0), (C*; Riello et al. 2021). An ideal case will show a 00000 flag.

The detailed analysis of the color-magnitude distance to the limiting 1.369 M_{\odot} relativistic and Newtonian tracks shown in the sixth and seventh columns, respectively, indicates that, on average, the selected faint blue branch objects are more compatible with the general relativistic model than with the Newtonian model. Six of them $\{a, b, c, f, g, m\}$ lie below the limiting 1.369 M_{\odot} relativistic track when they are 1σ compatible with the Newtonian model. Moreover, up to four objects $\{h, j, n, s\}$ are compatible with the relativistic model at the 1σ level but only marginally at a 2σ level with the Newtonian model. In particular, objects $\{j, s\}$ are ideal candidates to confirm relativistic models given that they present a 00000 flag, which is indicative of a reliable photometry and astrometry. The rest of the objects $\{d, i, k, o, p, r, t\}$ lie at a distance of 2σ or 3σ (the last two) for the relativistic model but at larger distances for the Newtonian model (up to 4σ). According to our study, these objects with such a small radius or larger masses would be unstable against gravitational collapse. However, any conclusion on this should be taken with caution. On one hand, although some of these objects belong to the sample analyzed by Bergeron et al. (2022) (d , J1612+5128; j , J1251+4403, also named WD1248+443 Harris et al. 2008; o , J1136–1057; and s , J0416–1826) and some near-infrared flux deficit has been reported for them, a more detailed spectroscopic analysis for all of our candidates is necessary for a precise mass and radius estimation. On the other hand, the presence of strong internal magnetic fields or a rapid rotation, not considered in this paper, could allow these objects to support the enormous gravity. It has been shown, in the general relativity framework, that including strong mag-

netic fields and/or a rapid rotation could lead to a smaller radius and/or a larger limiting mass for the most massive white dwarfs (for instance Boshkayev et al. 2013; Bera & Bhattacharya 2016; Subramanian & Mukhopadhyay 2015). The existence of super-Chandrasekhar white dwarfs, with masses of 2.1–2.8 M_{\odot} has indeed been proposed as a possible scenario to explain the over-luminous Type Ia supernovae SN 2003fg, SN 2006gz, SN 2007if, and SN 2009dc. A detailed follow-up of these objects is, in any case, deserved, and, at the same time, general relativistic models such as the ones presented in this work, but for white dwarfs with carbon-oxygen cores are expected to play a significant role in our understanding of the true nature of these objects.

5. Summary and conclusions

In this paper, we present the first set of constant rest-mass ultra-massive ONe white dwarf cooling tracks with masses of $M_{\star} > 1.29 M_{\odot}$, which fully take into account the effects of general relativity on their structural and evolutionary properties. Ultra-massive white dwarfs are relevant in different astrophysical contexts, such as type Ia supernovae explosions, stellar merger events, and the existence of high magnetic field white dwarfs. In addition, they provide insights into the physical processes in the super asymptotic giant branch phase preceding their formation. In the last few years, the existence of such ultra-massive white dwarfs in the solar neighborhood has been reported in several studies, including the recent discovery of a branch of faint blue white dwarfs in the color-magnitude diagram (Kilic et al. 2020; Scholz 2022). Although some of these objects present an infrared flux deficit, it is also thought to be composed of ultra-massive white dwarfs with masses larger than 1.29 M_{\odot} . It should be noted that it is very likely that g -mode pulsating ultra-massive white dwarfs with masses of $M_{\star} \geq 1.29 M_{\odot}$ will soon be discovered thanks to space missions such as the

Table 2. Ultra-massive white dwarf candidates selected from the sample of faint blue white dwarfs of Scholz (2022).

<i>Gaia</i> EDR3 source ID	$\varpi \pm \sigma_\varpi$ (mas)	$G \pm \sigma_G$ (mag)	$M_G \pm \sigma_{M_G}$ (mag)	$(G_{BP}-G) \pm \sigma_{(G_{BP}-G)}$ (mag)	Rel. model	New. model	Flags
6565940122868224640 ^a	11.717 ± 0.592	20.275 ± 0.005	15.619 ± 0.115	-0.008 ± 0.100	<1	1	00100
1983698716601024512 ^b	10.761 ± 0.934	20.549 ± 0.009	15.708 ± 0.198	-0.001 ± 0.084	<1	1	01000
6211904903507006336 ^c	15.411 ± 0.501	19.893 ± 0.006	15.832 ± 0.076	-0.014 ± 0.079	<1	1	00000 ¹
1424656526287583744 ^d	11.523 ± 0.685	20.668 ± 0.009	15.976 ± 0.138	-0.236 ± 0.150	2	2	11000 ¹
3585053427252374272 ^e	16.874 ± 0.464	20.054 ± 0.005	16.190 ± 0.065	-0.022 ± 0.070	1	1	01000 ¹
4377579209528621184 ^f	14.828 ± 0.860	20.379 ± 0.007	16.235 ± 0.133	0.043 ± 0.078	<1	1	01000
1505825635741455872 ^g	29.084 ± 0.190	19.022 ± 0.004	16.340 ± 0.018	0.041 ± 0.029	<1	1	00100 ^{1,2}
3480787358063803520 ^h	13.189 ± 1.365	20.769 ± 0.010	16.370 ± 0.235	-0.116 ± 0.132	1	2	11000
4461423190259561728 ⁱ	12.908 ± 2.082	20.829 ± 0.011	16.383 ± 0.361	-0.135 ± 0.096	2	2	01000
5064259336725948672^j	30.638 ± 0.219	19.005 ± 0.004	16.436 ± 0.019	0.027 ± 0.026	1	2	00000¹
534407181320476288 ^k	15.218 ± 0.640	20.533 ± 0.008	16.445 ± 0.099	-0.127 ± 0.080	2	3	01000
5763109404082525696 ^l	16.279 ± 0.949	20.424 ± 0.007	16.482 ± 0.134	-0.021 ± 0.136	1	1	11000 ¹
2858553485723741312 ^m	16.357 ± 0.715	20.452 ± 0.009	16.521 ± 0.104	0.026 ± 0.109	1	1	01000 ¹
6178573689547383168 ⁿ	17.098 ± 0.946	20.362 ± 0.009	16.527 ± 0.129	-0.057 ± 0.116	1	2	01000 ¹
3586879608689430400 ^o	17.572 ± 1.299	20.369 ± 0.007	16.593 ± 0.168	-0.193 ± 0.114	2	3	01000 ¹
1738863551836243840 ^p	19.444 ± 0.933	20.296 ± 0.007	16.740 ± 0.112	-0.117 ± 0.093	2	3	01000
6385055135655898496 ^q	16.607 ± 0.924	20.670 ± 0.009	16.771 ± 0.129	0.013 ± 0.130	1	1	11000
283928743068277376 ^r	27.731 ± 0.332	19.636 ± 0.004	16.850 ± 0.030	-0.133 ± 0.052	3	4	00100
152886174869458432^s	20.585 ± 0.614	20.325 ± 0.006	16.892 ± 0.070	-0.043 ± 0.082	1	2	00000^{1,3}
1674805012263764352 ^t	19.661 ± 1.347	20.792 ± 0.015	17.260 ± 0.164	-0.131 ± 0.076	3	4	01000

Notes. Sixth and seventh columns indicate the distance within the color diagram of Fig. 7 measured in 1σ deviations from the selected objects to the limiting $1.369 M_\odot$ cooling tracks for relativistic and Newtonian models, respectively. Objects *j* and *s*, marked in bold, are ideal candidates with no flags to confirm relativistic models. See text for rest of columns and details.

References. ¹Bergeron et al. (2022), ²Gates et al. (2004) ³Harris et al. (2008).

TESS and *Plato* space telescopes, and it will then be possible to study them through asteroseismology.

We computed the complete evolution of 1.29, 1.31, 1.33, 1.35, and $1.369 M_\odot$ hydrogen-rich white dwarfs models, assuming an ONe composition for the core. Calculations were performed using the La Plata stellar evolution code, LPCODE, for which the standard equations of stellar structure and evolution have been modified to include the effects of general relativity. To this end, we followed the formalism given in Thorne (1977). Specifically, the fully general relativistic partial differential equations governing the evolution of a spherically symmetric star are solved in a way that they resemble the standard Newtonian equations of stellar structure. For comparison purposes, the same sequences were computed, but for the Newtonian case. Our new white dwarf models include the energy released during the crystallization process, both due to latent heat and the induced chemical redistribution. We provide cooling times and time-dependent mass-radius relations for relativistic ultra-massive white dwarfs. We also provide magnitudes in *Gaia*, Sloan Digital Sky Survey and Pan-STARRS passbands, using the model atmospheres of Koester (2010), Koester & Kepler (2019). This set of cooling sequences, together with those calculated in Camisassa et al. (2019, 2022) for lower stellar masses than computed here, provide an appropriate theoretical framework to study the most massive white dwarfs in our Galaxy, superseding all existing calculations of such objects.

As expected, we find that the importance of general relativistic effects increases as the stellar mass is increased. According to our calculations, ONe white dwarfs more massive than $1.369 M_\odot$ become gravitationally unstable with respect to general relativity effects. When core chemical distribution due to phase separation on crystallization is considered, such instability occurs at somewhat lower stellar masses: $\gtrsim 1.360 M_\odot$. For our most massive sequence, the stellar radius becomes 25% smaller than predicted by the Newtonian treatment. The evolutionary properties

of our ultra-massive white dwarfs are also modified by general relativity effects. In particular, at advanced stages of evolution, the cooling times for our most massive white dwarf sequence are about a factor of two shorter than in the Newtonian case. In addition, not considering general relativity effects when estimating the properties of such objects through photometric and spectroscopic techniques would lead to an overestimation of their mass of $0.015 M_\odot$ near the critical mass.

In the color-magnitude diagram, we compare our theoretical sequences with the white dwarfs composing the faint blue white dwarf branch (Scholz 2022). We conclude that, regardless of the infrared deficit flux that some particular objects may exhibit, several white dwarfs of this branch can present masses larger than $\sim 1.29 M_\odot$ and that it does not coincide with any isochrone nor with any evolutionary track. We found that seven of the white dwarfs in this branch should have a smaller radius than our most massive cooling sequence and should be gravitationally unstable against collapse. However, apart from the need for a more detailed spectroscopic study to accurately characterize the possible effects of the infrared flux deficit in some of these objects, the presence of strong magnetic fields and a rapid rotation, not considered in this study, could favor the stability of such objects, thus supporting the existence of super-Chandrasekhar white dwarfs, that, in the case of CO-core white dwarfs, would likely be the progenitors of the over-luminous Type Ia supernovae SN 2003fg, SN 2006gz, SN 2007if, and SN 2009dc. Consequently, a detailed follow-up of these seven objects is required within the framework of the general relativity models exposed here.

As discussed throughout this work, our new ultra-massive white dwarf models for ONe core-chemical composition constitute an improvement over those computed in the framework of the standard Newtonian theory of stellar interiors. Therefore, in support of previous studies, the effect of general relativity must be taken into account to ascertain the true nature of the most

massive white dwarfs, and, in particular, to assess their structural and evolutionary properties.

Acknowledgements. We thank Detlev Koester for extending his atmosphere models to the high surface gravities that characterize our relativistic ultra-massive white dwarf models. We also thank the comments of an anonymous referee that improved the original version of this paper. Part of this work was supported by PICT-2017-0884 from ANPCyT, PIP 112-200801-00940 grant from CONICET, grant G149 from University of La Plata, NASA grants 80NSSC17K0008 and 80NSSC20K0193. S.T. and A.R.M. acknowledge support from MINECO under the PID2020-117252GB-I00 grant. A.R.M. acknowledges support from Grant RYC-2016-20254 funded by MCIN/AEI/10.13039/501100011033 and by ESF Investing in your future. R.R. has received funding from the postdoctoral fellowship program Beatrú de Pinós, funded by the Secretary of Universities and Research (Government of Catalonia) and by the Horizon 2020 programme of research and innovation of the European Union under the Maria Skłodowska-Curie grant agreement No. 801370. This research has made use of NASA Astrophysics Data System. This work has made use of data from the European Space Agency (ESA) mission *Gaia* (<https://www.cosmos.esa.int/gaia>), processed by the *Gaia* Data Processing and Analysis Consortium (DPAC, <https://www.cosmos.esa.int/web/gaia/dpac/consortium>). Funding for the DPAC has been provided by national institutions, in particular the institutions participating in the *Gaia* Multilateral Agreement.

References

- Althaus, L. G., Serenelli, A. M., Córscico, A. H., & Montgomery, M. H. 2003, *A&A*, 404, 593
- Althaus, L. G., Serenelli, A. M., Panei, J. A., et al. 2005, *A&A*, 435, 631
- Althaus, L. G., Córscico, A. H., Isern, J., & García-Berro, E. 2010, *A&ARv*, 18, 471
- Althaus, L. G., Camisassa, M. E., Miller Bertolami, M. M., Córscico, A. H., & García-Berro, E. 2015, *A&A*, 576, A9
- Althaus, L. G., Gil-Pons, P., Córscico, A. H., et al. 2021, *A&A*, 646, A30
- Bera, P., & Bhattacharya, D. 2016, *MNRAS*, 456, 3375
- Bergeron, P., Kilic, M., Blouin, S., et al. 2022, *ApJ*, 934, 36
- Blouin, S., & Daligault, J. 2021, *ApJ*, 919, 87
- Borucki, W. J., Koch, D., Basri, G., et al. 2010, *Science*, 327, 977
- Boshkayev, K., Rueda, J. A., Ruffini, R., & Siutsou, I. 2013, *ApJ*, 762, 117
- Bours, M. C. P., Marsh, T. R., Gänsicke, B. T., et al. 2015, *MNRAS*, 450, 3966
- Caiazzo, I., Burdge, K. B., Fuller, J., et al. 2021, *Nature*, 595, 39
- Camisassa, M. E., Althaus, L. G., Córscico, A. H., et al. 2019, *A&A*, 625, A87
- Camisassa, M. E., Althaus, L. G., Torres, S., et al. 2021, *A&A*, 649, L7
- Camisassa, M. E., Althaus, L. G., Koester, D., et al. 2022, *MNRAS*, 511, 5198
- Carvalho, G. A., Marinho, R. M., & Malheiro, M. 2018, *Gen. Relativ. Gravit.*, 50, 38
- Cheng, S., Cummings, J. D., & Ménard, B. 2019, *ApJ*, 886, 100
- Cheng, S., Cummings, J. D., Ménard, B., & Toonen, S. 2020, *ApJ*, 891, 160
- Christensen-Dalsgaard, J., Silva Aguirre, V., Cassisi, S., et al. 2020, *A&A*, 635, A165
- Córscico, A. H. 2020, *Front. Astron. Space Sci.*, 7, 47
- Córscico, A. H. 2022, ArXiv e-prints [arXiv:2203.03769]
- Córscico, A. H., Althaus, L. G., Miller Bertolami, M. M., & Kepler, S. O. 2019a, *A&ARv*, 27, 7
- Córscico, A. H., De Gerónimo, F. C., Camisassa, M. E., & Althaus, L. G. 2019b, *A&A*, 632, A119
- Curd, B., Gianninas, A., Bell, K. J., et al. 2017, *MNRAS*, 468, 239
- de Carvalho, S. M., Rotondo, M., Rueda, J. A., & Ruffini, R. 2014, *Phys. Rev. C*, 89, 015801
- De Gerónimo, F. C., Córscico, A. H., Althaus, L. G., Wachlin, F. C., & Camisassa, M. E. 2019, *A&A*, 621, A100
- Doherty, C. L., Siess, L., Lattanzio, J. C., & Gil-Pons, P. 2010, *MNRAS*, 401, 1453
- Gagné, J., Fontaine, G., Simon, A., & Faherty, J. K. 2018, *ApJ*, 861, L13
- Gaia* Collaboration (Babusiaux, C., et al.) 2018, *A&A*, 616, A10
- Gaia* Collaboration (Brown, A. G. A., et al.) 2021a, *A&A*, 649, A1
- Gaia* Collaboration (Smart, R. L., et al.) 2021b, *A&A*, 649, A6
- García-Berro, E., & Oswalt, T. D. 2016, *New Astron. Rev.*, 72, 1
- García-Berro, E., Ritossa, C., & Iben, I., Jr. 1997, *ApJ*, 485, 765
- Gates, E., Gyuk, G., Harris, H. C., et al. 2004, *ApJ*, 612, L129
- Gentile Fusillo, N. P., Tremblay, P. E., Cukanovaite, E., et al. 2021, *MNRAS*, 508, 3877
- Gianninas, A., Bergeron, P., & Ruiz, M. T. 2011, *ApJ*, 743, 138
- Gil-Pons, P., Suda, T., Fujimoto, M. Y., & García-Berro, E. 2005, *A&A*, 433, 1037
- Haft, M., Raffelt, G., & Weiss, A. 1994, *ApJ*, 425, 222
- Harris, H. C., Gates, E., Gyuk, G., et al. 2008, *ApJ*, 679, 697
- Hermes, J. J., Kepler, S. O., Castanheira, B. G., et al. 2013, *ApJ*, 771, L2
- Hollands, M. A., Tremblay, P. E., Gänsicke, B. T., et al. 2020, *Nat. Astron.*, 4, 663
- Howell, S. B., Sobek, C., Haas, M., et al. 2014, *PASP*, 126, 398
- Isern, J., Torres, S., & Rebassa-Mansergas, A. 2022, *Front. Astron. Space Sci.*, 9, 6
- Itoh, N., Hayashi, H., Nishikawa, A., & Kohyama, Y. 1996, *ApJS*, 102, 411
- Jiménez-Esteban, F. M., Torres, S., Rebassa-Mansergas, A., et al. 2018, *MNRAS*, 480, 4505
- Kanaan, A., Kepler, S. O., Giovannini, O., & Diaz, M. 1992, *ApJ*, 390, L89
- Kepler, S. O., Pelisoli, I., Koester, D., et al. 2016, *MNRAS*, 455, 3413
- Kilic, M., Bergeron, P., Kosakowski, A., et al. 2020, *ApJ*, 898, 84
- Kilic, M., Bergeron, P., Blouin, S., & Bédard, A. 2021, *MNRAS*, 503, 5397
- Kippenhahn, R., Weigert, A., & Weiss, A. 2012, *Stellar Structure and Evolution* (Berlin, Heidelberg: Springer)
- Kleinman, S. J., Kepler, S. O., Koester, D., et al. 2013, *ApJS*, 204, 5
- Koester, D. 2010, *Mem. Soc. Astron. It.*, 81, 921
- Koester, D., & Kepler, S. O. 2019, *A&A*, 628, A102
- Lindegren, L., Hernández, J., Bombrun, A., et al. 2018, *A&A*, 616, A2
- Magni, G., & Mazzitelli, I. 1979, *A&A*, 72, 134
- Mathew, A., & Nandy, M. K. 2017, *Res. Astron. Astrophys.*, 17, 061
- Medin, Z., & Cumming, A. 2010, *Phys. Rev. E*, 81, 036107
- Miller Bertolami, M. M. 2016, *A&A*, 588, A25
- Moriya, T. J. 2019, *MNRAS*, 490, 1166
- Moya, A., Barceló Forteza, S., Bonfanti, A., et al. 2018, *A&A*, 620, A203
- Mukadam, A. S., Mullally, F., Nather, R. E., et al. 2004, *ApJ*, 607, 982
- Nitta, A., Kepler, S. O., Chené, A.-N., et al. 2016, *IAU Focus Meeting*, 29, 493
- Nunes, S. P., Arbañil, J. D. V., & Malheiro, M. 2021, *ApJ*, 921, 138
- Piotto, G. 2018, *European Planetary Science Congress, EPSC2018-969*
- Pshirkov, M. S., Dodin, A. V., Belinski, A. A., et al. 2020, *MNRAS*, 499, L21
- Ricker, G. R., Winn, J. N., Vanderspek, R., et al. 2015, *J. Astron. Telesc. Instrum. Syst.*, 1, 014003
- Riello, M., De Angeli, F., Evans, D. W., et al. 2021, *A&A*, 649, A3
- Rotondo, M., Rueda, J. A., Ruffini, R., & Xue, S.-S. 2011, *Phys. Rev. D*, 84, 084007
- Rowan, D. M., Tucker, M. A., Shappee, B. J., & Hermes, J. J. 2019, *MNRAS*, 486, 4574
- Salaris, M., Althaus, L. G., & García-Berro, E. 2013, *A&A*, 555, A96
- Schol, R.-D. 2022, *Res. Notes Am. Astron. Soc.*, 6, 36
- Schwab, J. 2021a, *ApJ*, 916, 119
- Schwab, J. 2021b, *ApJ*, 906, 53
- Segretain, L., Chabrier, G., Hernanz, M., et al. 1994, *ApJ*, 434, 641
- Siess, L. 2006, *A&A*, 448, 717
- Siess, L. 2010, *A&A*, 512, A10
- Silva Aguirre, V., Christensen-Dalsgaard, J., Cassisi, S., et al. 2020, *A&A*, 635, A164
- Subramanian, S., & Mukhopadhyay, B. 2015, *MNRAS*, 454, 752
- Temink, K. D., Toonen, S., Zapartas, E., Justham, S., & Gänsicke, B. T. 2020, *A&A*, 636, A31
- Thorne, K. S. 1977, *ApJ*, 212, 825
- Torres, S., Canals, P., Jiménez-Esteban, F. M., Rebassa-Mansergas, A., & Solano, E. 2022, *MNRAS*, 511, 5462
- Tremblay, P.-E., Fontaine, G., Fusillo, N. P. G., et al. 2019, *Nature*, 565, 202
- Ventura, P., & D'Antona, F. 2011, *MNRAS*, 410, 2760
- Winget, D. E., & Kepler, S. O. 2008, *ARA&A*, 46, 157
- Wu, C., Xiong, H., & Wang, X. 2022, *MNRAS*, 512, 2972